Fluid Dynamics &
Materials Processing

Tech Science Press

http://doi.org/10.32604/fdmp.2026.083338

ARTICLE

Transient Multiphase CFD Investigation of Piston Cooling Galleries: Effects of Inlet Angle and Guide Vane Geometry

Fei Dong, Weichao Zhang, Jiurui Zhao and Tongwei Zhang*

School of Automotive and Traffic Engineering, Jiangsu University, 301 Xuefu Road, Zhenjiang, China
*Corresponding Author: Tongwei Zhang. Email: zhtw@ujs.edu.cn

Received: 02 April 2026; Accepted: 05 June 2026; Published: 30 June 2026

ABSTRACT: Internal cooling galleries are widely employed to mitigate piston thermal loads in gasoline engines, where their configuration plays a critical role in temperature distribution and component durability. In this study, Cradle CFD was coupled with the Conjugate Heat Transfer (CHT) and Volume of Fluid (VOF) multiphase approaches to investigate the effects of inlet angle and guide vane geometry on piston thermal performance. The SST k-ω turbulence model was adopted to resolve the transient flow behavior associated with reciprocating motion, while the Box-Behnken design methodology was applied to develop empirical correlations for optimization. The results demonstrate that an inlet angle of 10° delivers the most effective thermal performance, reducing the maximum and minimum piston temperatures by 1.69°C and 28.34°C, respectively, while also producing the highest heat transfer coefficient. In contrast, a 15° inlet angle promotes excessive turbulence and flow instability, leading to diminished cooling effectiveness. For the inlet geometry, the configuration defined by L_1 = 1.15 mm and L_2 = 16.3 mm achieves the highest area-averaged heat transfer coefficient of 1755.13 W/(m^2·K) at 270°CA. Subsequent response surface optimization identifies L_1 = 2.3 mm and L_2 = 14.0 mm as the optimal design parameters, corresponding to a time-averaged heat transfer coefficient of 1928.513 W/(m^2·K).

KEYWORDS: Piston; heat transfer; cooling channel; multiphase flow

1 Introduction

In order to meet the requirements of energy saving and emission reduction of automobile engines, the increasing load puts forward higher requirements for the temperature and life of engine pistons. The piston ensures the structural stability, reasonable matching, reliable lubrication, and efficient combustion process of the internal combustion engine [1–3]. Various piston cooling channel structures are widely used in the design of pistons to provide high cooling efficiency [4,5]. The cooling performance of the internal cooling oil cavity is affected by many factors, such as the flow state of the oil, the inlet momentum, the structure of the oil cavity, and the thermal boundary conditions. Optimizing its design has become one of the hot issues in the research of piston thermal management [6].

The heat transfer process inside the piston is essentially a multi-phase non-steady-state heat transfer system driven by high-frequency reciprocating motion. In the internal cooling oil cavity, the oil does not flow continuously and stably but oscillates significantly under the periodic movement of the piston, forming a dynamic redistribution. This oscillating flow is particularly complex in the environment where the gas-liquid two phases coexist [7]. In order to deeply understand the behavior of the oil in the oil cavity, researchers have widely adopted CFD technology, supplemented by experimental verification, and

constructed a multi-physical field coupling model to accurately simulate the internal flow and heat transfer process. The cooling capacity of the liquid in the oil cavity depends not only on its temperature and flow rate but more importantly on its contact state and flow pattern with the wall [8]. Under the influence of reciprocating motion, the liquid tends to accumulate on the upper wall during the downward stroke of the piston, forming a liquid film area, which brings the largest heat transfer coefficient; while the oil moves downward when the piston moves upward, and the cooling center of gravity shifts to the lower wall, making the heat transfer coefficient change dynamically with time and space [9]. This asymmetric heat exchange process needs to be specially considered in design optimization. On the other hand, the influence of wettability on heat transfer efficiency has also received increasing attention.

New methods for enhancing heat transfer have also been proposed. Qin et al. [10] introduced nano-fluid technology, which effectively improved the thermal conductivity of engine oil by adding high thermal conductivity nano-particles (such as Al_2O_3 and CuO) to the engine oil, and the nano-particles enhanced the wall scouring effect, further enhancing the turbulent heat transfer effect. Malathi et al. [11] introduced a secondary flow mechanism driven by multi-frequency oscillation in the simulation and found that a more uniform oil coverage distribution can be formed in the cavity, which improves the uniformity of heat flux. These advances have laid a solid foundation for the theoretical improvement and practical application of piston thermal management.

The oil cavity inlet area plays a role in fluid guidance in the entire cooling system, and its structural design plays a decisive role in the flow pattern, wall scouring behavior, and heat transfer path after the oil enters [12]. In recent years, scholars have gradually realized that the influence of the inlet structure on the heat transfer efficiency cannot be ignored, and related research has gradually increased, but the overall is still in the early stage of development. From the perspective of the inlet, its change will directly change the flow direction and momentum vector distribution after the oil is injected. Dhairiyasamy et al. [13] studied the influence of different inlet angles on the flow path and vortex structure of the oil through numerical simulation and found that when the angle is set to 10°, the oil can be effectively guided to flow forward along the cavity in a spiral shape, avoiding the formation of the back-flow area, so that a larger heat flux density is generated in the outlet area. When the angle is too small (such as 0°), the oil tends to move in a straight line in the cavity and cannot cover more wall areas, while when the angle is too large (such as above 20°), it is easy to cause unstable impact adhesion, back-flow, and even local oil accumulation, which reduces the heat transfer efficiency. In terms of inlet size design, short and wide structures have been proven to have better heat transfer characteristics. Mehtab et al. [14] pointed out that the short and wide inlet can aggravate the fluid disturbance in the initial stage of the oil entering the oil cavity, induce a stronger turbulent structure, destroy the formation of the boundary layer, and thus improve the local heat transfer coefficient; at the same time, a stronger momentum gradient can be established in the inlet area to accelerate the distribution of the oil to the deep part of the cavity. Dizisaz et al. [15] further studied the influence of the inlet cross-sectional shape on the flow symmetry and found that the rectangular inlet is conducive to the film flow of the liquid along the inner wall of the cavity, while the circular or sharp-angled structure is more likely to form a velocity vortex core area, resulting in flow instability.

In addition, the multi-inlet structure is also one of the current research hot-spots. The double-jet inlet structure proposed by Wang et al. [16] significantly improved the uniformity and flow stability of the oil coverage in the cavity through symmetrical injection. The actual measurement results show that the heat transfer coefficient is increased by 13.3%, the maximum temperature of the oil cavity is reduced by 7°C, and the thermal stress distribution of the piston is effectively improved. This design concept not only optimizes

the flow path of the oil in the entire cavity but also reduces the hot “dead zone” area, which is an important direction for structural innovation.

The flow and heat transfer inside the reciprocating cooling gallery involve complex transient liquid-gas two-phase fluid mechanics, widely known as the “cocktail shaker” effect. Over the past decades, numerous researchers have carried out numerical and experimental investigations to understand this phenomenon. Yoshikawa and Reitz [17] developed an improved multi-phase oil gallery cooling model by comprehensively considering this cocktail shaker effect, validating that the combination of cyclic inertial forces and fluid sloshing deeply alters the heat flux distribution. To quantify these local phenomena, Torregrosa et al. [18] contributed a rigorous experimental methodology for estimating film heat transfer coefficients inside Diesel engine cooling galleries, revealing the sensitivity of local cooling performance to the engine’s operational speed. Similarly, Najafabadi et al. [19] coupled experimental validation with a three-dimensional computational fluid dynamics (CFD) approach to reveal how the spatial alignment of the fluid jet interacts with different reciprocating positions of the piston to dominate the heat transfer boundaries.

To further enhance the cooling efficiency of the gallery, optimizing the structural parameters and surface topography has attracted significant attention. Yu et al. [20] established an advanced visualization test rig to directly observe the forced-oscillation flow patterns of the oil-air interface, clarifying the critical relationship between fluid distribution and regional heat dissipation. Considering that the interior surfaces of manufactured galleries are not perfectly smooth, Hamza et al. [21] thoroughly evaluated the effect of surface roughness elements, such as dimples and protrusions, indicating that micro-topographies distort the oil slug formation and influence the localized jet impingement zone. In parallel with internal channel modifications, broad research on external surface features has shown that geometric modifications can significantly boost regional thermal performance. For instance, Kumar et al. [22] verified that introducing protruded structures within heat exchanger channels remarkably augments the local Nusselt numbers through vortex generation. Narato et al. [23] numerically and experimentally investigated the influence of inclined cylindrical pin arrays on the fluid flow, proving that specific inclination angles generate optimal secondary flows that minimize boundary layer thermal resistance. Furthermore, Leontiev et al. [24] demonstrated that utilizing dimpled surfaces with distinct shapes (e.g., spherical, oval, teardrop) can drastically optimize the trade-off between heat transfer enhancement and fluidic drag force.

Although there have been a large number of research results on the flow and heat transfer behavior inside the piston, most of the research still focuses on the macroscopic flow path or the overall oil cavity structure optimization, and the guiding mechanism of the “inlet structure” as the starting point of the flow on the subsequent heat transfer process is less discussed. The inlet area is the first contact surface for the power input of the oil. Whether the structural design is reasonable or not will determine the flow mode and cooling intensity distribution of the coolant inside the cavity. Therefore, the inherent coupling relationship between the inlet structure and the heat transfer performance of the oil cavity needs to be further revealed.

Therefore, in view of the above-mentioned research deficiencies, this study explores the influence of the inlet angle and the shape parameters of the inlet structure and optimizes the structure. The surface of the piston oil passage is divided into different areas, and the flow and heat transfer process in the oil passage is simulated in detail, including the oil flow state and the distribution of the heat transfer coefficient under different crankshaft angles. This study innovatively proposes a cooling oil cavity inlet structure adjustment and optimization scheme: on the one hand, the inlet angle is changed to optimize the distribution of oil in the oil passage; on the other hand, the oil flow is optimized by changing the inlet structure, which provides a basis for further research on piston temperature changes. The influence of the inlet angle and structure

of the piston internal cooling oil cavity studied in this paper on the piston temperature field is of great significance.

2 Models and Methods

2.1 Geometric Model

As shown in Fig. 1, the Z1 area of the piston oil cavity is defined as the inlet area, The inlet region Z1 is located at the lower part of the cooling gallery, where the cooling oil enters the cavity. The orientation of the inlet passage relative to the piston axis is defined by the inlet angle θ, which will be discussed in detail in Section 3.1 and the Z7 area is defined as the outlet area. The oil cavity wall surface is divided into inner wall surface, outer wall surface, upper wall surface, and lower wall surface according to the spatial position: the inner wall surface and the outer wall surface respectively correspond to the part of the oil cavity close to the piston center and the outer edge, that is, the corresponding area of the inner side and the outer side of the piston; the upper wall surface and the lower wall surface are respectively the top and bottom of the oil cavity, corresponding to the corresponding positions of the top and skirt of the piston. This division method provides a structured basis for the refined analysis of the flow characteristics and cooling effect inside the oil cavity. Given the significant spatial heterogeneity of the oil flow velocity field and temperature field near different wall surfaces, this zoning strategy can reveal the flow-heat transfer correlation mechanism of each wall surface area in a targeted manner and then provide key support for the overall cooling performance evaluation of the piston and the analysis of the heat load distribution characteristics.

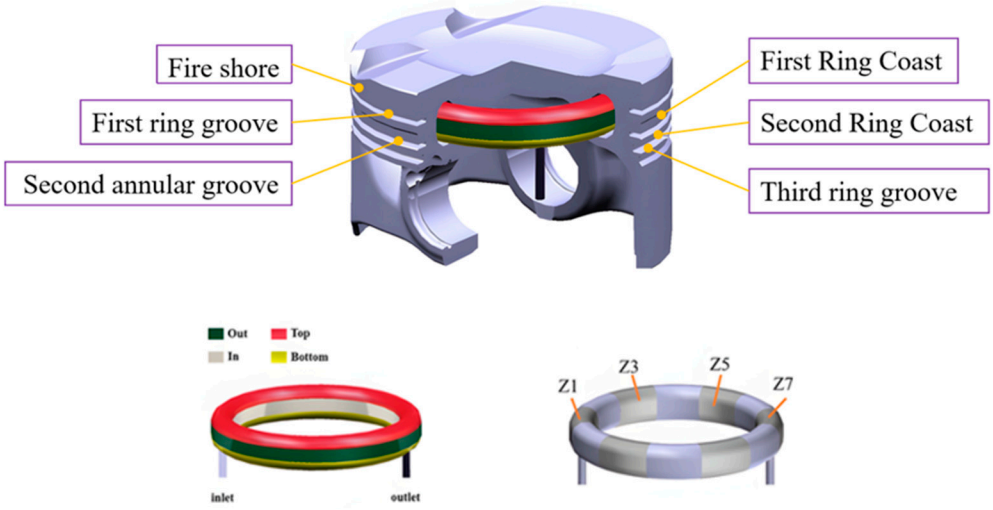

Figure 1: Piston model.

2.2 Physical Processes and Assumptions

In the numerical simulation, a reasonable simulation model was established, and the complexity of the oil flow and heat transfer in the cooling oil passage was taken into account. This study simplified some aspects and established a calculation model. Based on previous studies [25,26], several logical assumptions were adopted to simplify the CFD model:

(1) Air was assumed to be an ideal gas.
(2) Engine oil was regarded as an incompressible fluid, and its surface tension was assumed to be independent of temperature.

(3) It was assumed that oil and air were immiscible or could not be mixed. The cooling oil cavity was regarded as a movable rigid body.

2.3 Conservation Equations

2.3.1 Governing Equations

The transient fluid flow and heat transfer inside the piston cooling gallery are governed by the classical conservation laws. The mass conservation (continuity) equation is expressed as follows Eq. (1) [27]:

$$\nabla \cdot \vec{u} = 0 \tag{1}$$

$\vec{u}$ is the fluid velocity vector. This equation ensures the mass conservation within the computational domain.

The momentum conservation equation (Navier-Stokes equation) is shown in Eq. (2) [27]:

$$\rho \frac{\partial \mathrm{u}}{\partial t} + \rho(\mathrm{u} \cdot \nabla)\mathrm{u} = -\nabla p + \nabla \cdot \tau + \nabla \cdot \tau_R + \rho \mathrm{g} + \mathrm{F}_s \tag{2}$$

ρ is the fluid density, p is the pressure, g is the gravitational acceleration vector, $\tau = \mu\left[\nabla u + (\nabla u)^T\right]$ represents the molecular viscous stress tensor for a Newtonian fluid. $\tau_R = \mu_t\left[\nabla u + (\nabla u)^T\right]$ represents the Reynolds turbulent stress tensor used for turbulence closure. F_s denotes the volumetric surface tension force acting historically on the phase interface, which is detailed in Section 2.3.2.

The energy conservation equation is shown in Eq. (3) [27]:

$$\rho \frac{\partial e}{\partial t} + \rho \nabla \cdot (ue) = -\nabla \cdot q + \nabla \cdot (\tau \cdot u) + \rho Q_s \tag{3}$$

where the heat flux vector is defined as $q = -\left(\lambda + \frac{C_p \mu_t}{Pr_t}\right)\nabla T$, λ is the effective thermal conductivity and Pr_t is the turbulent Prandtl number, as there is no internal heat source, Q_s in the system is set to 0.

This equation indicates that the rate of change of the fluid's energy is equal to the sum of heat conduction, viscous dissipation, and heat source.

2.3.2 Multiphase Flow Model

In this study, the fluid domain comprises two immiscible phases: engine oil (liquid phase) and air (gas phase). To track the complex, transient sharp interface between the two phases due to the reciprocating motion, the Volume of Fluid (VOF) method is adopted. In the VOF framework, the distribution of phases is represented by the phase variable F (the volume fraction of the liquid phase in each computational cell). The tracking of the interface is achieved by solving the passive scalar transport equation for F (4) [28]:

$$\frac{\partial F}{\partial t} + \nabla \cdot (Fu) = 0 \tag{4}$$

where $F = 1$ indicates a cell completely filled with engine oil, $F = 0$ indicates a cell filled with air, and $0 < F < 1$ represents the interface transition region.

The effective physical properties (density ρ and dynamic viscosity μ) in any localized cell are determined by a linear volume-averaging formulation based on the phase variable F (5) [28]:

$$\rho = F\rho_l + (1 - F)\rho_g, \mu = F\mu_l + (1 - F)\mu_g \tag{5}$$

where the subscripts l and g denote the independent physical properties of the liquid phase (oil) and gas phase (air).

Furthermore, the boundary momentum source term F_s caused by surface tension in the momentum equation is modeled using the Continuum Surface Force (CSF) approach Eq. (6) [27]:

$$F_s = \sigma k \nabla F \tag{6}$$

where σ is the surface tension coefficient, and k is the local surface curvature computed from the divergence of the unit normal of the interface: $k = -\nabla \cdot (\nabla F / |\nabla F|)$.

2.3.3 Turbulence Equations

In this study, the gravitational acceleration g = 9.81 m/s^2 is incorporated into the momentum equation to account for its influence on oil distribution and interface evolution during reciprocating motionthe, and the SST k-ω turbulence model is adopted to accurately capture the complex flow field characteristics induced by the reciprocating movement of the piston. This model has significant advantages in transient flow simulation under moving boundary conditions and can accurately analyze the secondary flow, flow separation, and vortex evolution process dominated by inertial force in the oil cavity during the acceleration and deceleration stages of the piston and can reliably predict the dynamic change law of wall shear stress and local heat transfer coefficient.

The SST k-ω model constants are specified as: $\sigma_k = 1.0, \sigma_w = 1.176, \alpha = 0.52, \beta = 0.075, \beta^* = 0.09$.

Turbulent viscosity (μ_t):

$$\mu_t = \frac{\rho k}{\omega}$$

The turbulent kinetic energy equation of the k-ω model is shown in (7) [28]:

$$\frac{\partial(\rho k)}{\partial t} + \frac{\partial(\rho k u_i)}{\partial x_i} = \frac{\partial}{\partial x_j}\left[\left(\mu + \frac{\mu_t}{\sigma_k}\right)\frac{\partial k}{\partial x_j}\right] + G_k - \beta \rho k \omega \tag{7}$$

ω represents the turbulent frequency, which represents the time scale of the turbulent vortex, and β represents the empirical constant. This equation describes the transport process of turbulent kinetic energy k, which is similar to the turbulent kinetic energy equation of the k-ε model, but the dissipation term is represented by $\beta \rho k \omega$, which reflects the influence of the turbulent frequency ω on the dissipation of turbulent kinetic energy.

The turbulent frequency ω equation is shown in (8) [29]:

$$\frac{\partial(\rho \omega)}{\partial t} + \frac{\partial(\rho \omega u_i)}{\partial x_i} = \frac{\partial}{\partial x_j}\left[\left(\mu + \frac{\mu_t}{\sigma_\omega}\right)\frac{\partial \omega}{\partial x_j}\right] + \alpha \frac{G_k}{v_t} - \beta \rho \omega^2 \tag{8}$$

This equation describes the transport process of the turbulent frequency ω, including the time-varying term, the convection term, the diffusion term, the generation term and the dissipation term. The generation term $\alpha \frac{G_k}{v_t}$ represents the effect of turbulent kinetic energy generation on the turbulent frequency, and the dissipation term $\beta \rho \omega^2$ represents the self-dissipation of the turbulent frequency.

$$\mu_t = \lambda_1\left(\frac{G_k}{\omega}\right), \sigma_\omega = \lambda_2\left(\frac{G_k}{\omega}\right) \tag{9}$$

where G_k is the turbulent gradient, λ_1 and λ_2 are correction functions.

The expression for the heat transfer coefficient in the model is as follows (10) [28]:

$$h = \frac{q_i}{T_i - T_w} \tag{10}$$

where h is the wall heat transfer coefficient, T_i is the temperature of the i phase, T_w is the wall temperature. The average heat transfer coefficient h_w over an area A of the wall is calculated using the following Eq. (11) [28]:

$$h_w = \frac{1}{T}\int_0^T \left(\frac{1}{A}\int_A h dA\right) dt \tag{11}$$

where A is the surface area within the oil passage, T is the period of one complete reciprocating cycle of the piston.

2.3.4 Numerical Solution Settings

The transient simulations were performed using a pressure-based solver with the PISO (Pressure-Implicit with Splitting of Operators) algorithm for pressure-velocity coupling, which is well-suited for transient multiphase flows with large time-step sizes. The PRESTO (PREssure STaggering Option) scheme was used for pressure discretization, while second-order upwind schemes were employed for momentum, turbulent kinetic energy, and turbulent frequency. The Geo-Reconstruct scheme was applied for volume fraction discretization to achieve sharp interface capturing.

A variable time-stepping strategy was adopted with an initial time step of 1×10^{-5} s, limited by a maximum Courant number of 0.5 to ensure numerical stability. The convergence criteria for each time step were set as 10^{-4} for continuity, momentum, and volume fraction equations, and 10^{-5} for energy and turbulence equations. Each time step required 20–30 iterations to achieve convergence. The piston motion was implemented using a dynamic mesh with a layering approach, where cells near the moving boundaries were added or removed based on the piston position updated by the crank-slider mechanism.

The engine operating condition was set at 300 rpm with an oil supply pressure of 0.3 MPa and temperature of 90°C. A total of 10 reciprocating cycles were simulated to achieve periodic steady-state conditions, with the last cycle used for data analysis.

2.4 Boundary Conditions

The physical properties of the lubricating oil used in the simulation are summarized in Table 1. The density, specific heat capacity, dynamic viscosity, and thermal conductivity were set as constant values due to the relatively narrow temperature variation range of the oil during the cooling process. The simulation process accumulates 10 movement cycles of the piston to ensure the periodic stability of the flow field.

Table 1: Physical properties of engine oil.

Parameters	Value
Density (kg/m^3)	857
Specific heat capacity (kJ/(kg·K))	2.019
Dynamic viscosity (Pa·s)	0.01733
Thermal conductivity (W/(m·K))	0.1303

The accurate description of the piston thermal boundary conditions needs to consider the thermal conductivity of the piston material, the flow state of the working medium, and the speed of the piston movement. The geometric structure and thermal boundary conditions are shown in Fig. 1 and Table 2 respectively.

Table 2: The third kind of thermal boundary condition of piston.

Region	Temperature (°C)	Heat Transfer Coefficient (W/(m^2·K))
Top surface	850	415
Fire shore	675	290
First Ring Coast	180	1400
First ring groove	180	1400
Second Ring Coast	120	1000
Second annular groove	120	1000
Third ring groove	100	800
skirt	50	300

2.5 Grid Independence Verification and Model Validation

Grid independence tests were performed to ensure the accuracy of the simulation results in this paper. Since this paper studies the flow and heat transfer process in the piston cooling channel, the heat transfer coefficient distribution on the upper surface of the piston cooling channel can be regarded as a decisive factor. As shown in Fig. 2, the comparison of heat transfer coefficient distributions on the upper surface of the cooling gallery for three mesh resolutions: 300,000, 400,000, and 500,000 cells. Obviously, these specific grid distributions produced basically the same results. In the subsequent calculations in this paper, the 400,000 cells was selected as the model grid number.

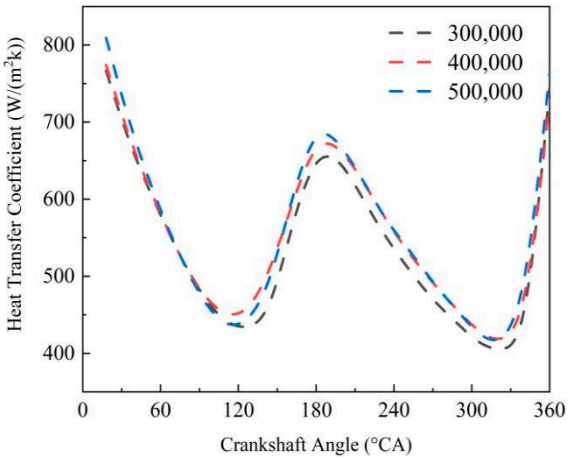

Figure 2: Model grid independence verification.

The computational domain was discretized using polyhedral unstructured grids with prism layer meshes near wall surfaces to resolve boundary layer flows. Grid independence was verified using three mesh resolutions: 0.3×10^6, 0.4×10^6, and 0.5×10^6 cells. The 0.4×10^6-cell mesh was selected for subsequent calculations, as further refinement to 0.5×10^6 cells produced negligible differences (<2%) in the area-averaged heat transfer coefficient on the upper wall surface (Figs. 3 and 4). Special attention was paid to the inlet region and wall boundaries: the minimum cell size near the inlet was 0.05 mm to capture

complex multiphase flow behavior, and 5 prism layers were generated on all wall surfaces with a growth ratio of 1.2 and first layer thickness of 0.01 mm, ensuring $y^+ < 1$ for accurate boundary layer resolution. The maximum cell skewness was 0.85, and the orthogonal quality was above 0.15, meeting the solver requirements.

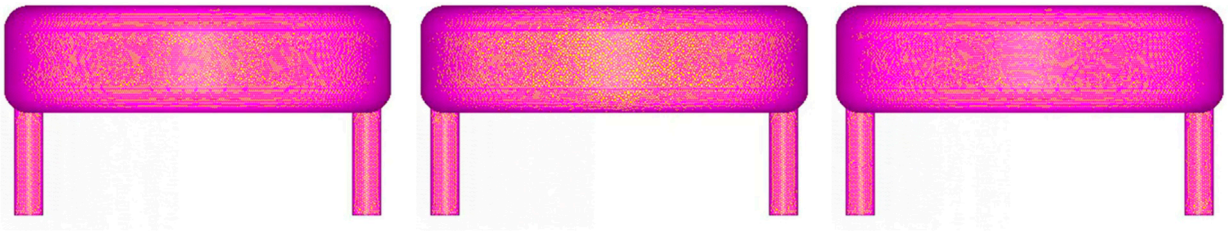

(**a**) 300,000 (**b**) 400,000 (**c**) 500,000

Figure 3: Mesh modeling of cooling oil passages with different number of meshes.

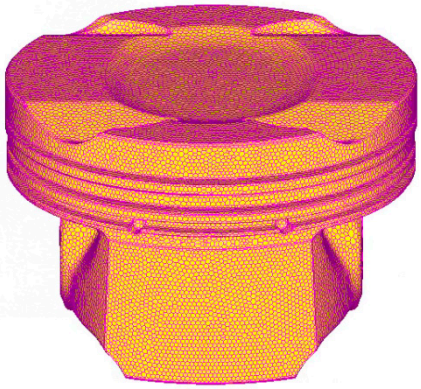

Figure 4: Piston mesh model.

This study employed the experimental apparatus established by Dong et al. [29] to compare the movement of engine oil within oil passages with simulation models. The experimental setup is shown in the Fig. 5. During the experiment, the oil passage underwent reciprocating motion at 300 rpm, as illustrated in Fig. 6. The blue regions in the figure represent the gas phase, while the red regions denote the liquid phase. At crankshaft angles of 90° and 180°, oil columns formed within the oil chamber, with air accumulating on either side of these columns. As the oscillation duration increased, bubbles gradually formed within the chamber. Quantitative validation was performed by comparing the oil phase distribution along the centreline of the channel under 90°CA and 180°CA conditions. As shown in Table 3, the normalised root-mean-square deviation (NRMSD) between the experimental and simulated oil volume fraction distribution curves was 8.5% at 90°CA and 12.3% at 180°CA, indicating good agreement between the two. The slight deviation at 180°CA may be attributed to uncertainties in the processing of experimental images, as well as the idealised assumption of constant oil supply pressure in the simulation. The numerical simulations and experimental results exhibited consistent trends, validating the accuracy of the simulation.

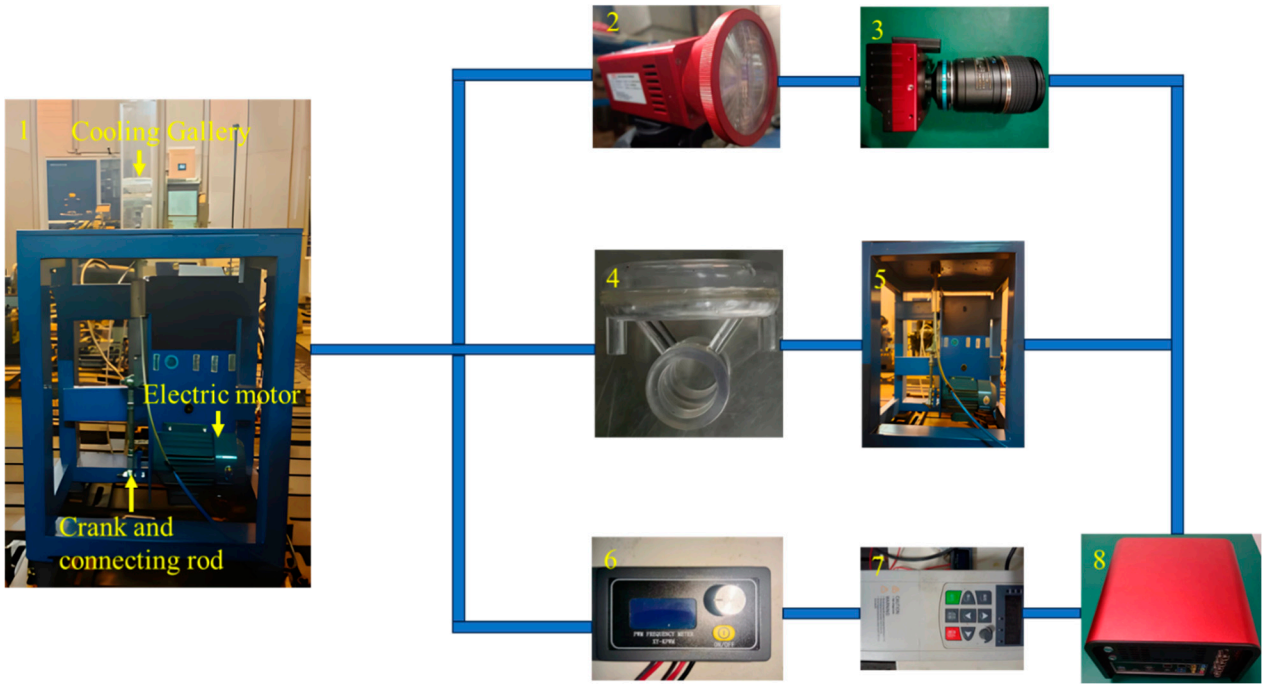

Figure 5: Experimental setup diagram (**1**. equipment layout, **2**. light source, **3**. high-speed camera, **4**. cooling oil chamber, **5**. drive motor, **6**. Flowmeter, **7**. Controller, **8**. signal processor).

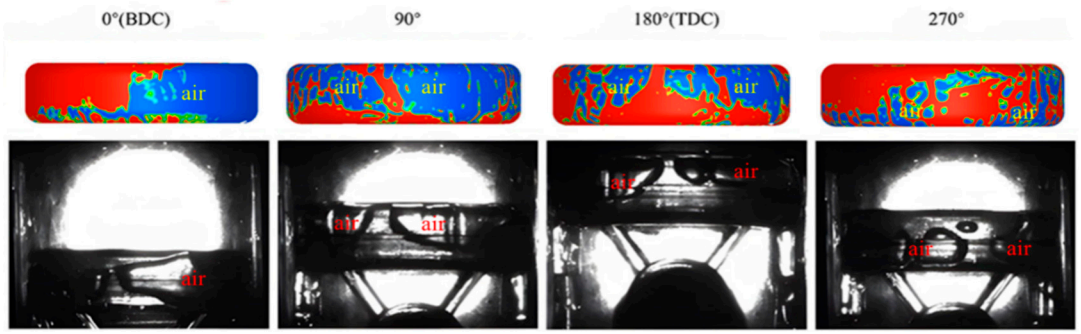

Figure 6: Model validation.

Table 3: Error analysis.

Crank Angle	NRMSD (%)	Maximum Deviation (%)
90°CA	8.5	15.2
180°CA	12.3	22.1

3 Results and Discussion

3.1 Influence of Different Inlet Angles

3.1.1 Influence of Inlet Angle on Piston Temperature Field

This study compares and analyzes the influence of the inlet angle on the piston temperature field. As shown in Fig. 7, the inlet angle θ is defined as the angle between the centerline of the cooling gallery inlet passage and the piston vertical axis (aligned with the cylinder bore axis). Fig. 7a shows the location of

the inlet region (Z1) at the lower part of the piston oil cavity. Fig. 7b presents a detailed cross-sectional view of the inlet geometry, where θ is measured in the plane containing the piston vertical axis and the inlet centerline. The baseline configuration has $\theta = 0^\circ$ (vertical inlet, i.e., the inlet centerline is parallel to the piston axis), and parametric variations include $\theta = 5^\circ$, 10°, and 15° (Fig. 7c). During the parametric study, all other geometric parameters (inlet length L_1, inlet width L_2, and gallery cross-section) remain constant to isolate the effect of inlet angle. A suitable inlet angle can enhance the turbulence intensity of the oil, promote full contact between the oil and the oil cavity wall, and thereby improve the heat transfer efficiency. By reasonably adjusting the inlet angle, the internal temperature distribution of the piston can be improved, the local overheating phenomenon can be reduced, the risk of thermal stress and thermal fatigue can be reduced, and the service life of the piston can be prolonged.

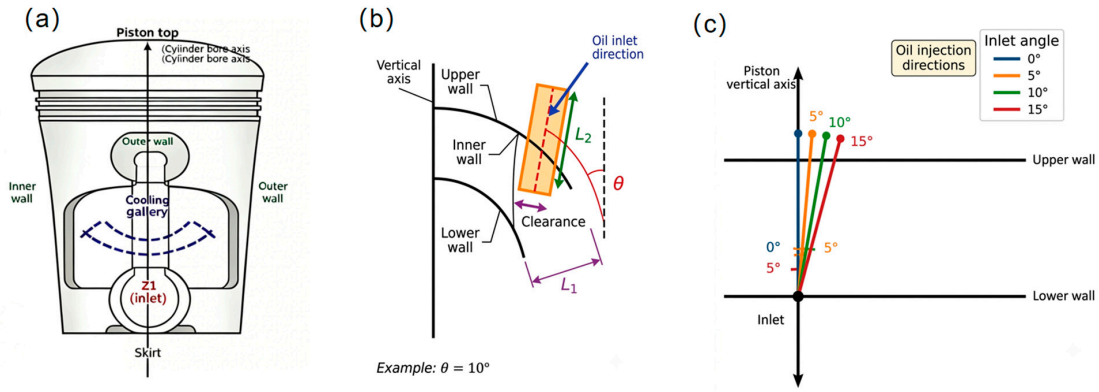

Figure 7: Schematic definition of the cooling gallery inlet angle θ. (**a**) Location of the inlet region (Z1) in the piston oil cavity; (**b**) Detailed view of the inlet geometry showing the angle θ measured between the inlet centerline and the piston vertical axis (parallel to the cylinder bore); (**c**) Cross-sectional view illustrating the oil injection direction.

Fig. 8 compares the distribution of the piston temperature field with the inlet inclination angle of 0° and 10°. It is found that the maximum temperature difference between the two is 1.69°C after the inclination angle is changed, and the minimum temperature is below the skirt, with a difference of 28.34°C. It shows that the inlet angle has an impact on the distribution of the piston temperature field.

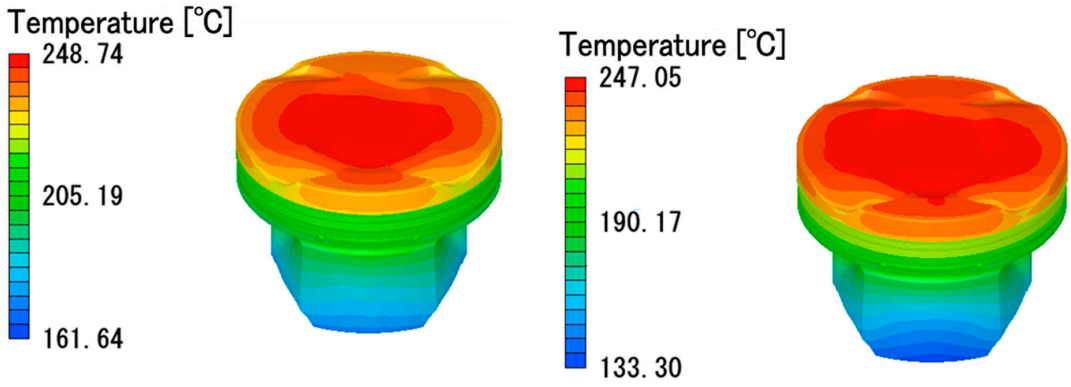

(**a**) Tilt angle 0° (**b**) Tilt angle 10°

Figure 8: Piston temperature field distribution diagram.

Fig. 9 shows the average temperature of the four inlet angle pistons, which is 11°C lower than the initial temperature. The piston temperature is the lowest when the inclination angle is 10°, which is 201.8°C, and the difference from the highest temperature is 10°C. This shows that the change of oil cavity structure can further reduce the piston temperature distribution, avoid the aggravation of thermal load, and improve the piston life.

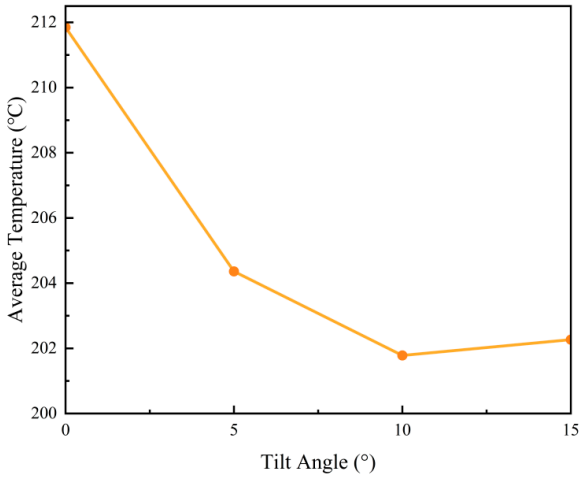

Figure 9: Average piston temperature.

As shown in Fig. 10, the average temperature of different parts after 10 cycles of piston movement is compared. The temperature fluctuation of the piston top surface is relatively gentle, which is mainly due to the position of the internal cooling oil cavity. The cooling oil cavity is close to the high-temperature area at the top of the piston, and the forced convection heat exchange effectively stabilizes the top surface temperature. In contrast, the temperature change of the fire shore and the first ring groove is more significant. When the piston runs to the bottom dead center, a large amount of splashed oil accumulates on the outer wall of the piston to form a local oil film. The axial distance between this position and the fire shore and the ring groove is short, which leads to the heat in these two areas being mainly taken away by the oil film through lateral conduction. The change range is significantly larger than that of the piston top surface.

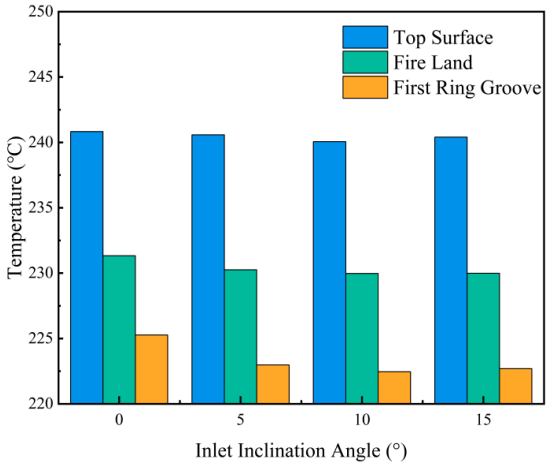

Figure 10: Comparison of the average temperature of different parts of the piston.

3.1.2 Influence of Inlet Angle on Wall Heat Transfer Coefficient

As shown in Fig. 11, the average heat transfer coefficient of the wall surface changes under different angles of the inlet of the internal cooling oil passage. It is found from the figure that the overall heat transfer coefficient of the internal cooling oil passage is larger when the inclination angle is 10°, because the inclined oil cavity inlet will change the direction of the oil flow and form a large flow disturbance. This disturbance will promote the fluid in the oil cavity to enter the turbulent state. In the turbulent flow, the laminar boundary layer of the fluid is thinned, which accelerates the uniform distribution of heat in the oil cavity.

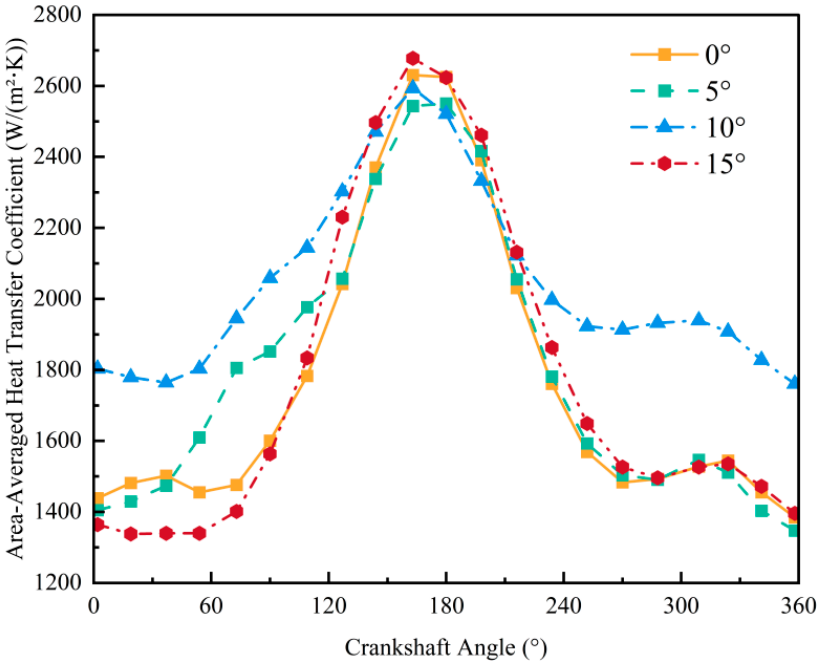

Figure 11: Average heat transfer coefficient of the wall surface of the cooling gallery at different inclination angles.

However, an excessive angle will lead to excessive turbulence enhancement, which may cause flow instability. This excessive turbulence may not only lead to flow separation but also make the flow in the oil cavity irregular, which reduces the effective contact time between the oil and the piston surface, thereby reducing the local heat transfer efficiency. An excessive inclination angle will also increase the pressure loss of the oil flow. Especially at high flow rates, the fluid needs to overcome greater resistance to flow through the oil cavity. A large pressure loss will reduce the overall cooling efficiency of the system, which will affect the heat transfer. The average heat transfer coefficient of different wall surfaces of the piston is compared and analyzed below.

As shown in Fig. 12, the area heat transfer coefficient of the lower wall surface area of the internal cooling oil passage changes. Due to the different distribution states of the engine oil on each wall surface at different times, the change states of the area heat transfer coefficient of each wall surface are different. When the internal cooling oil passage moves to the vicinity of the bottom dead center, the area heat transfer coefficient of the lower wall surface appears. The peak value, the inner wall surface, and the upper wall surface appear as peaks near the top dead center. The area heat transfer coefficient of the inner wall surface is large before and after the bottom dead center, and the curve appears as a trough near the top dead center.

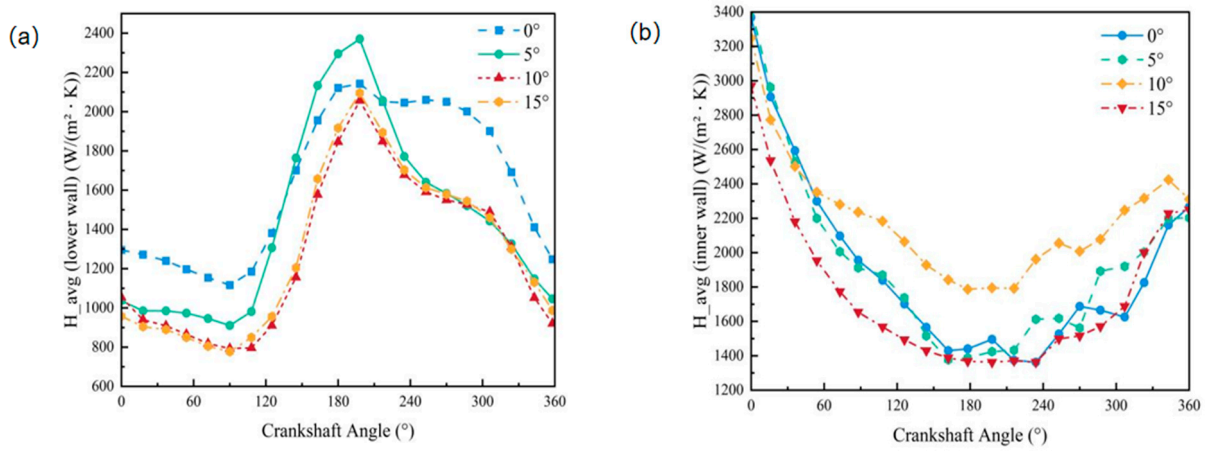

Figure 12: Area-averaged heat transfer coefficients of (**a**) the bottom wall and (**b**) the inner wall of the cooling gallery at different inlet inclination angles.

In Fig. 13, the peak value of the outer wall surface appears when the crankshaft angle is about 60°CA, and then it shows a downward trend until 300°CA. The area heat transfer coefficient curve of the upper wall surface is similar to that of the inner wall surface. The maximum value appears at about 0°CA, and the minimum value appears at about 90°CA. In the area heat transfer coefficient diagram of the four wall surfaces, the heat dissipation effect of the inclination angle of 10° is the highest as a whole, and the change of the inclination angle of the inlet of the inner cooling oil passage can indeed improve the heat dissipation effect. When the inner cooling oil passage starts to move, the difference of the area heat transfer coefficient under different inclination angles is not large due to the inconspicuous oscillation degree. As the crankshaft angle increases, the oil oscillation in the cavity becomes violent, and the heat transfer coefficient appears to be different.

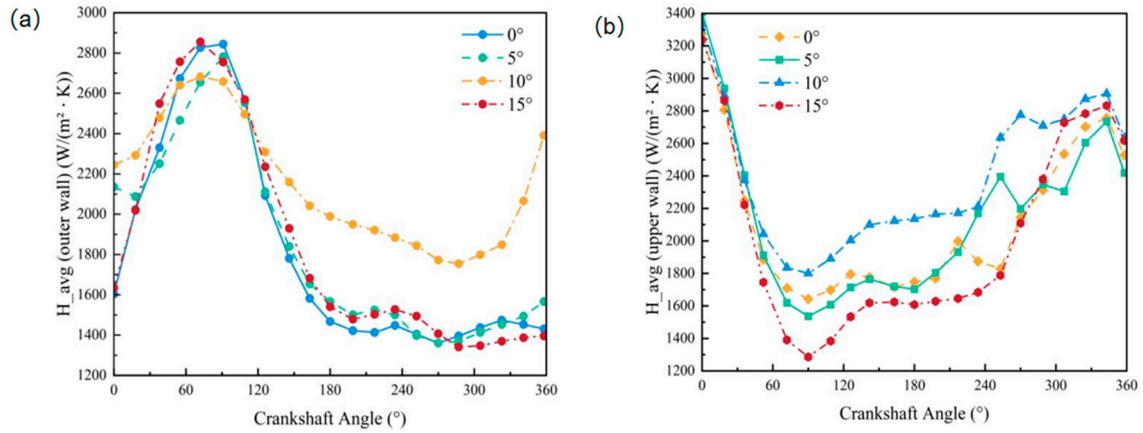

Figure 13: Area-averaged heat transfer coefficients of (**a**) the outer wall and (**b**) the upper wall of the cooling gallery at different inlet inclination angles.

3.1.3 Influence of Inlet Angle on Engine Oil Distribution

As shown in Fig. 14, the oil distribution of the section of the cooling oil passage inlet at different angles of the top dead center, in which the oil of the cooling oil passage with a 10° inclination angle almost fills the inlet section, and there is no obvious air cavity or local oil cut-off area. This high filling state allows the

oil to enter the oil passage with a stable flow rate and low resistance, fully covering the high-temperature components near the top dead center. Compared with other inclination angles, the contact between the oil and the high-temperature surface is more sufficient under the 10° design, the thermal conductivity is significantly improved, and the cooling effect is better than other angle schemes.

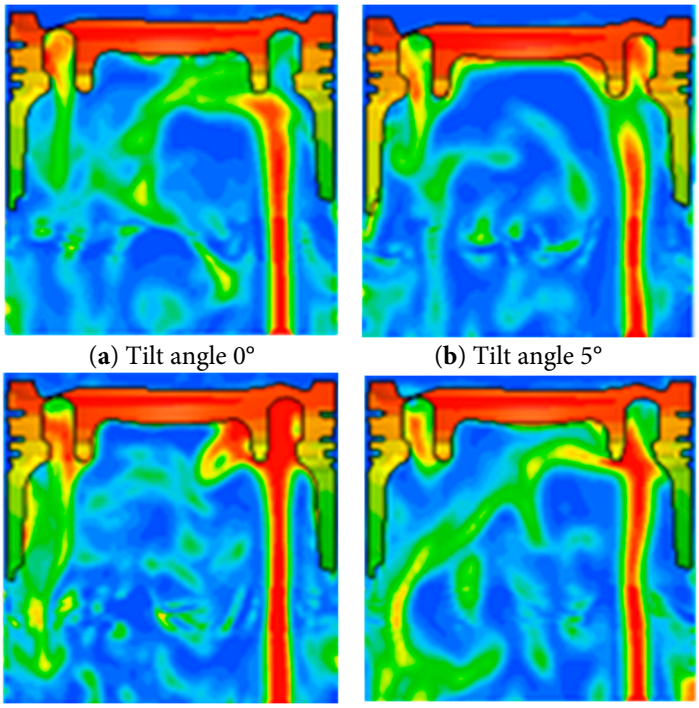

(**a**) Tilt angle 0° (**b**) Tilt angle 5°

(**c**) Tilt angle 10° (**d**) Tilt angle 15°

Figure 14: Distribution of VOF at different angles of the cooling channel inlet at the TDC.

In Fig. 15, the oil distribution of the inner cooling oil passage at different times under different inclination angles is shown. When the crankshaft angle is 270°, more droplets are gathered at the oil cavity inlet with an angle of 10°. By comparing the droplet distribution at each moment, it is found that more droplets enter the oil cavity during the downward movement, indicating that the increase of the angle can improve the speed of droplets entering the oil cavity to a certain extent, thereby accelerating the piston cooling and improving the cooling efficiency.

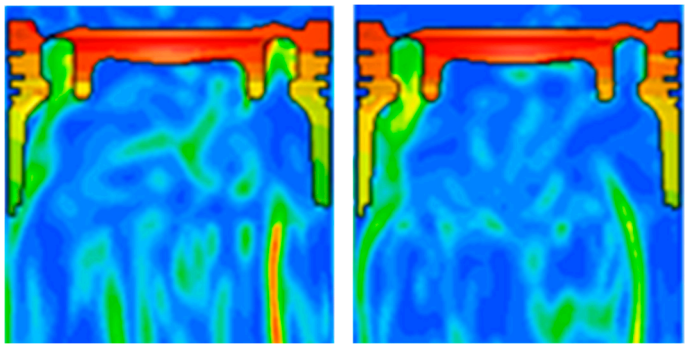

(**a**) Tilt angle 0° (**b**) Tilt angle 5°

Figure 15: *Cont.*

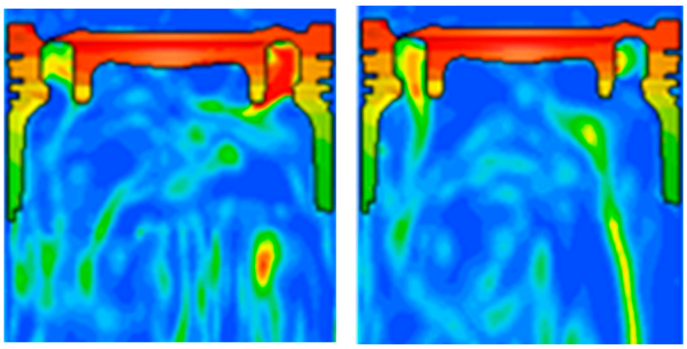

(**c**) Tilt angle 10° (**d**) Tilt angle 15°

Figure 15: VOF distribution of cooling oil channel inlet at different angles of 270°CA.

As shown in Fig. 16, the VOF distribution diagram of the cooling oil passage with different inlet angles shows that the oil is mainly concentrated on the inner and outer wall surfaces at 0°CA; the oil on the upper wall surface begins to increase at 90°CA;a large amount of oil washes the upper wall surface when the piston runs to the top dead center, that is, at 180°CA; and the inclination angle is the most obvious at 10°.

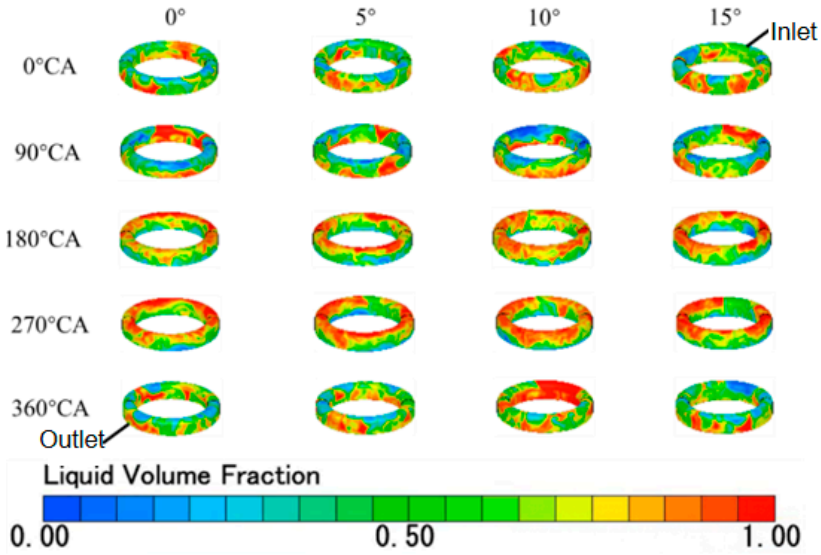

Figure 16: Cooling oil gallery VOF distribution.

When running downward from 180°CA, because the direction of piston speed is opposite to the direction of oil, the oil always stays on the upper wall surface. When the angle is 10°, the oil at the inlet is more than the other three, which also leads to the heat transfer coefficient near the inlet at 270°CA and 360°CA in Fig. 17, which is significantly higher than other regions.

The above analysis shows that the piston cooling efficiency is increased by injecting oil from different inlet angles, but the excessive angle will affect the heat transfer coefficient of the wall surface and the distribution of oil in the section. The cooling effect is the best when the inlet angle is 10°, the heat transfer coefficient of the wall surface is increased by 16%, and the average temperature is reduced by 10°.

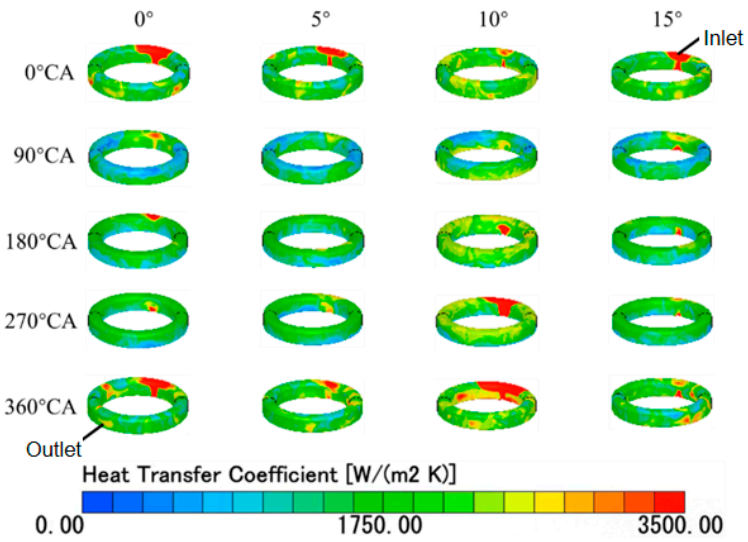

Figure 17: Heat transfer coefficient distribution of Cooling Oil Gallery.

Table 4 summarizes the key performance indicators for the four inlet angles. The 10° inlet angle consistently outperforms other configurations across all metrics: it achieves the lowest maximum piston temperature (201.8°C), the highest cycle-averaged heat transfer coefficient (1624 W/(m^2·K)), and the most complete oil coverage at TDC (92%). While 15° produces higher turbulence intensity, the associated flow instability reduces the effective cooling. The 0° and 5° angles result in insufficient wall coverage, particularly on the upper wall during the downward stroke.

Table 4: Comparison of cooling performance for different inlet angles.

Parameter	0°	5°	10°	15°
Maximum piston temperature (°C)	203.49	203.0	201.8	202.5
Minimum piston temperature (°C)	95.0	88.0	66.66	72.0
Average piston temperature (°C)	212.0	208.5	201.8	206.0
Temperature uniformity index (°C)	108.49	115.0	135.14	130.5
Peak area-averaged HTC on bottom wall (W/(m^2·K))	1250	1380	1520	1480
Peak area-averaged HTC on inner wall (W/(m^2·K))	1180	1290	1450	1380
Peak area-averaged HTC on outer wall (W/(m^2·K))	1320	1450	1620	1550
Peak area-averaged HTC on upper wall (W/(m^2·K))	1280	1410	1580	1490
Cycle-averaged HTC of gallery (W/(m^2·K))	1400	1510	1624	1530
Oil coverage at TDC (%)	72	78	92	85

3.2 Influence of Different Inlet Shapes

This study compares the influence of the change of inlet structure parameters on the heat transfer efficiency of the oil cavity. As shown in Fig. 18, the inlet structure of the cooling oil cavity of this model is shown. The inlet of the internal cooling oil passage is approximately regarded as a polygon, and the inlet length and inlet width are set as parameters L_1 and L_2. Latin hypercube is used to sample parameters L_1 and L_2. The value range of each parameter is equally divided into several non-overlapping intervals, and a sample point is randomly selected in each interval. At the same time, the arrangement rule of the Latin square is used to ensure that the sample combination of all parameter dimensions is evenly distributed in the projection space. A total of 11 schemes were designed, as shown in Table 5, and simulated and analyzed.

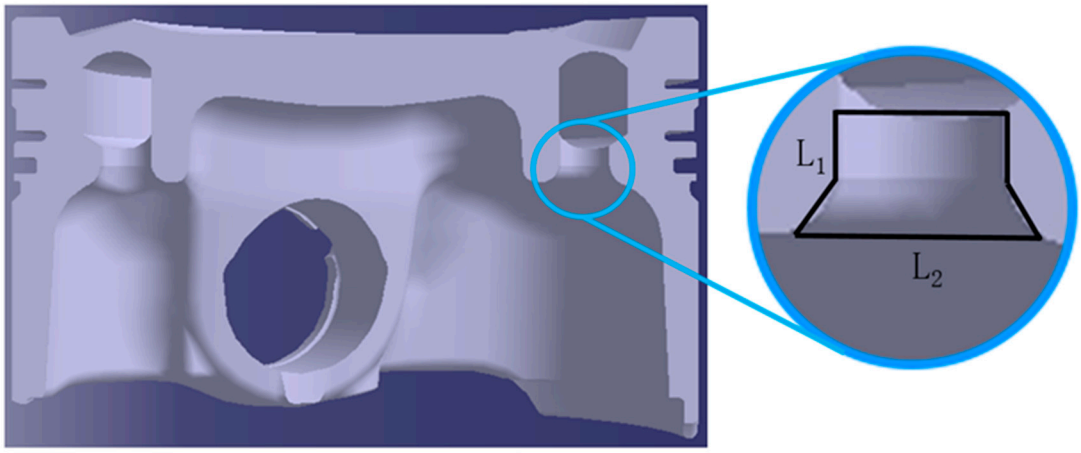

Figure 18: Parameters of inlet structure of cooling gallery.

Table 5: Structural parameter design schemes.

Case	L_1 (mm)	L_2 (mm)
1	1.10	17.2
2	1.15	16.3
3	1.25	15.7
4	1.35	15.1
5	1.60	13.5
6	1.70	12.9
7	1.85	12.0
8	1.95	11.4
9	2.10	10.4
10	2.20	9.8
11	2.30	9.2

In Fig. 19, the area heat transfer coefficient of the inner cooling oil cavity wall surface changes with different structural parameters. Except for the crankshaft rotation angle of 180°, the area average heat transfer coefficient of scheme 2 is higher than that of other schemes at the other four moments. The shorter the inlet length L_1, the shorter the path through which the droplets pass, the more the friction resistance is reduced, the more the average flow rate is increased, and the more quickly the oil reaches the entire oil passage surface, avoiding the loss of too much energy during the inflow process.

The greater the width of inlet L_2, the larger the inlet area becomes. At a constant flow velocity, a higher flow rate into the oil passage facilitates oil film formation, increases the contact area between droplets and the oil chamber walls, and enhances heat exchange efficiency. Increasing the inlet width facilitates a higher oil inflow rate, enabling cooling oil to rapidly enter the oil passages and establish a stable flow field within. This allows the oil to cover larger high-temperature areas within the piston in a shorter time frame, increasing the contact area between the oil and the inner walls of the oil passages, thereby enhancing heat transfer efficiency.

Reducing the inlet length minimizes pressure loss as oil enters the oil chamber, enhancing flow efficiency and ensuring more uniform oil distribution within the chamber. A short inlet length combined with a wider inlet allows cooling oil to disperse rapidly and evenly throughout the entire oil chamber. This mitigates uneven oil distribution, ensuring effective coverage of the cooling surface. Conversely, a

short and wide inlet exacerbates fluid disturbance, generating increased turbulence. Turbulence effectively disrupts the fluid boundary layer, reducing laminar flow thickness and minimizing stagnant zones. This prevents thermal efficiency degradation caused by oil pooling in specific areas, facilitating more efficient heat transfer from the oil chamber walls to the cooling oil.

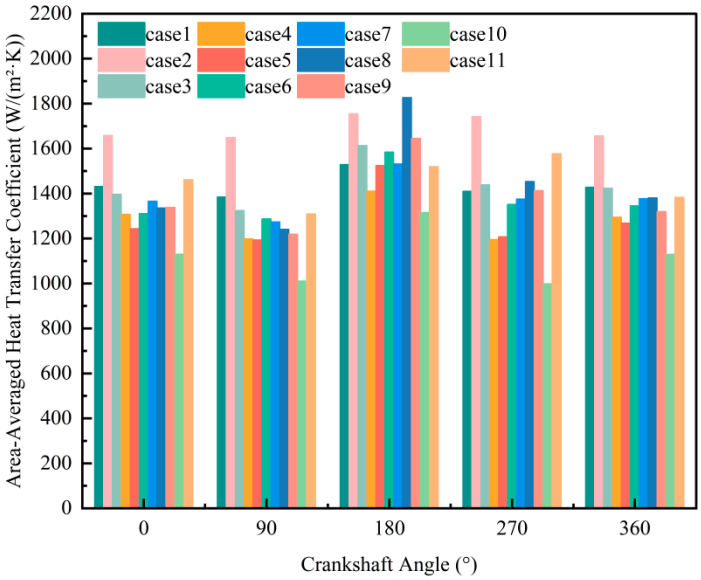

Figure 19: Heat transfer coefficients of wall surface area of cooling gallery under different structural parameters.

Fig. 20 illustrates the liquid-phase flow state within the piston cross-section cooling oil passages at a 0° crankshaft angle, under different structural parameters. The right side represents the cooling oil passage inlet, while the left side denotes the outlet. It can be observed that only in Scheme 2 does the oil fill the entire inlet of the oil channel. In Scheme 4, the oil volume at the inlet is reduced, with only a few oil droplets adhering to the outer wall surface to form an oil film. In Scheme 10, the majority of the oil remains near the lower wall surface, obstructing droplet entry into the oil channel inlet.

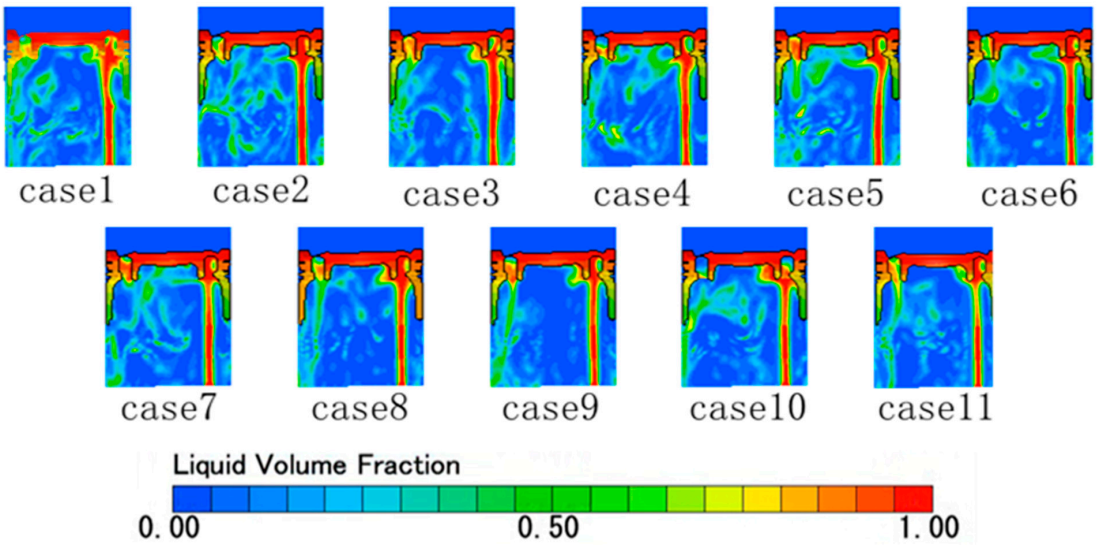

Figure 20: 0° crankshaft angle oil flow state of the internal coolant gallery with different structural parameters.

As shown in Fig. 21, the liquid phase flow state within the piston cross-section's internal cooling oil passages at a 180° crankshaft angle varies with different structural parameters. At 180° crankshaft angle, Scheme 2 exhibits the highest oil volume at the inlet. However, as the piston reaches top dead centre, only a small quantity of oil flows into the oil chamber inlet. Scheme 3 and Scheme 6 retain residual oil, while other model schemes exhibit minor oil distribution near the inlet. At the top dead centre position, the piston's velocity reaches its maximum before rapidly decelerating and reversing direction. This high-speed motion causes the oil, under inertia, to lag behind the piston's movement, particularly at the inlet of the piston cooling oil cavity. The oil flow is significantly impacted by the piston's rapid motion, resulting in a transient 'interruption' phenomenon.

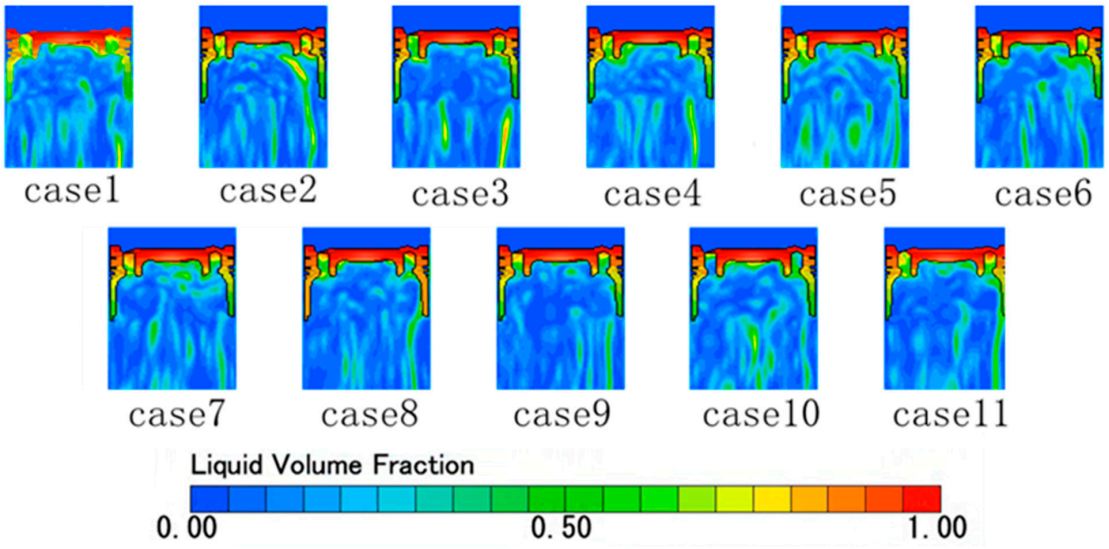

Figure 21: 180° crankshaft angle oil flow state of the internal coolant gallery with different structural parameters.

Near the top dead centre, the piston's vigorous motion disrupts oil flow. As the piston approaches its highest position, its velocity peaks before abruptly decelerating and accelerating in the opposite direction. This sudden change in speed prevents the oil from keeping pace with the piston due to inertia. Particularly at the inlet region of the cooling oil chamber, the high-speed piston causes a momentary interruption in oil flow.

Concurrently, the piston's rapid movement significantly alters the trajectory of oil splashing. The abrupt change in piston direction deflects the oil stream originally directed towards the oil chamber, causing substantial droplets to be flung onto other piston surfaces rather than the intended cooling area. This flow deviation directly reduces the effective oil volume entering the oil chamber.

As shown in Fig. 22, the VOF distribution within the cooling oil channels under different structural parameters is depicted. At 0°CA, schemes 2, 3, 7, and 9 exhibit a greater concentration of droplets. At 90°CA, schemes 5, 6, and 10 show virtually no oil on the upper wall surface. When the piston moves downward, oil oscillation within the oil chamber intensifies, with a more pronounced oil distribution on the upper wall surface.

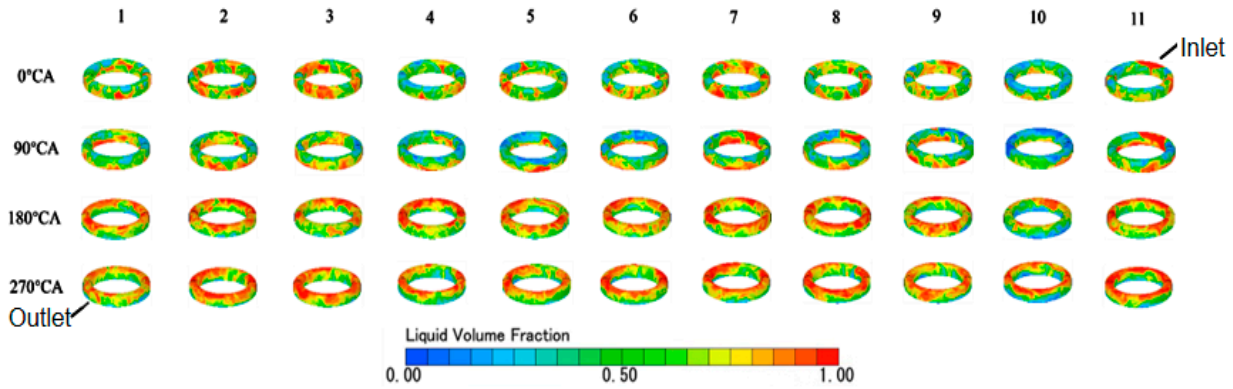

Figure 22: Distribution of VOF in cooling oil gallery with different structures.

Fig. 23 illustrates the distribution of heat transfer coefficients across cooling oil channels under varying structural parameters. The diagram clearly demonstrates that Scheme Two consistently delivers superior overall heat transfer performance at different time points compared to the other schemes.

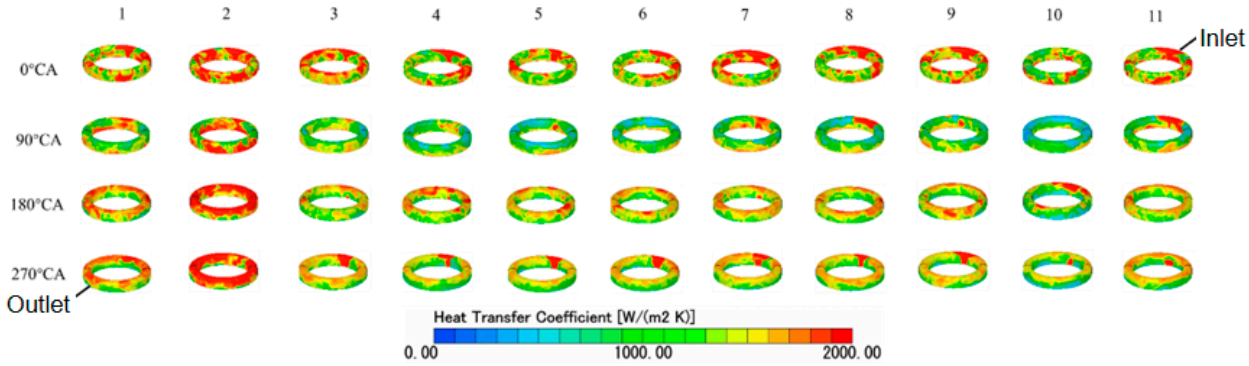

Figure 23: Heat transfer coefficient distribution in cooling oil gallery with different structures.

The above analysis demonstrates that modifying the inlet structure enhances piston cooling efficiency. Among the variants, Option Two (L_1-1.15, L_2-16.3) achieves the highest heat transfer efficiency across the piston wall surface, exceeding other variants by over 13%. This ensures greater oil coverage area at different points in time compared to alternative configurations, thereby maximizing avoidance of oil flow interruption.

3.3 Optimization of Inlet Structure Parameters

The Box-Behnken design (BBD) was employed to establish the response surface model for the time-averaged heat transfer coefficient. Two factors were considered: inlet length L_1 and inlet width L_2. Based on preliminary simulations and manufacturing constraints, three levels were defined for each factor (Table 6).

Table 6: Factor levels for Box-Behnken design.

Factor	Symbol	Low (−1)	Center (0)	High (+1)
Inlet length (mm)	L_1	1.1	1.7	2.3
Inlet width (mm)	L_2	9.2	13.2	17.2

The BBD requires 13 experimental runs including 4 center points for reproducibility assessment. However, considering the discrete nature of practical manufacturing, 11 representative schemes were selected from the design space for CFD simulation (Table 7).

Table 7: Box-Behnken design matrix and responses.

Case	L_1 (mm)	L_2 (mm)	Coded L_1	Coded L_2	h_w (W/(m^2·K))
1	1.10	17.2	−1.000	1.000	1892.24
2	1.15	16.3	−0.907	0.775	1841.97
3	1.25	15.7	−0.750	0.625	1785.34
4	1.35	15.1	−0.583	0.475	1738.64
5	1.60	13.5	−0.167	0.075	1647.34
6	1.70	12.9	0.000	−0.075	1610.70
7	1.85	12.0	0.250	−0.300	1526.33
8	1.95	11.4	0.417	−0.450	1503.11
9	2.10	10.4	0.667	−0.700	1488.70
10	2.20	9.8	0.833	−0.850	1458.76
11	2.30	9.2	1.000	−1.000	1441.32

This study optimized the inlet structure parameters. As shown in Fig. 24, the time-weighted average heat transfer coefficient was calculated for the average heat transfer coefficient across the internal cooling oil channel area under different parameters. Based on the obtained data, an empirical formula was fitted using the Box-Behnken method, and a response surface was plotted. A response surface was constructed by systematically selecting experimental points across high, medium, and low levels of each factor while avoiding extreme combinations. Analysis of the response contour plot revealed that the heat transfer coefficient gradually decreased with increasing L_1 and decreasing L_2.

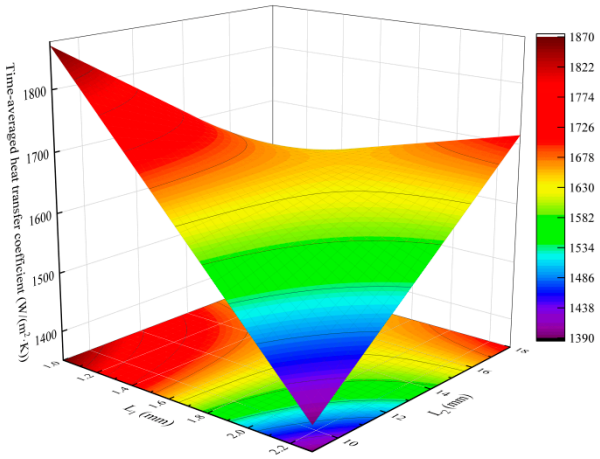

Figure 24: Response plots of time-averaged heat transfer coefficients of cooling gallery within different structural parameters.

Fig. 25 presents the residual verification of the model alongside comparisons between predicted and actual values. Observation reveals that external studentized residuals cluster predominantly near a straight line, indicating residuals largely follow a normal distribution and demonstrating the model sound adaptability. Predicted values fluctuate around actual values, exhibiting high consistency between the two. In summary, the model exhibits excellent adaptability and consistency with actual values.

Furthermore, the time-averaged heat transfer coefficient data undergoes objective optimization using a multi-objective optimization algorithm. This algorithm constitutes a decision-making methodology for resolving multi-objective optimization problems, particularly suited to scenarios where multiple objectives conflict or where simultaneous satisfaction of multiple constraints is required. Its core principle involves defining deviations between the objective function and its ideal values, then minimizing these deviations to identify the optimal solution.

In target planning, upper and lower deviations are introduced to measure the gap between target values and ideal values. Weights or priorities are assigned based on the importance of different objectives, ensuring optimal compromise across all targets while minimizing deviations. The algorithm's advantages include effective handling of multi-objective balancing, highly flexible model adjustment capabilities, and ease of comprehension and implementation. With the time-averaged heat transfer coefficient as the optimization target, optimal structural parameters were obtained. L_1 = 2.3 mm, L_2 = 14.0 mm, with a time-averaged heat transfer coefficient of 1928.513 W/(m^2·K). By substituting these optimal structural parameters into the model for calculation, the time-averaged heat transfer coefficient under these parameters is determined to be 2054.9 W/(m^2·K), representing an error of 6.6%.

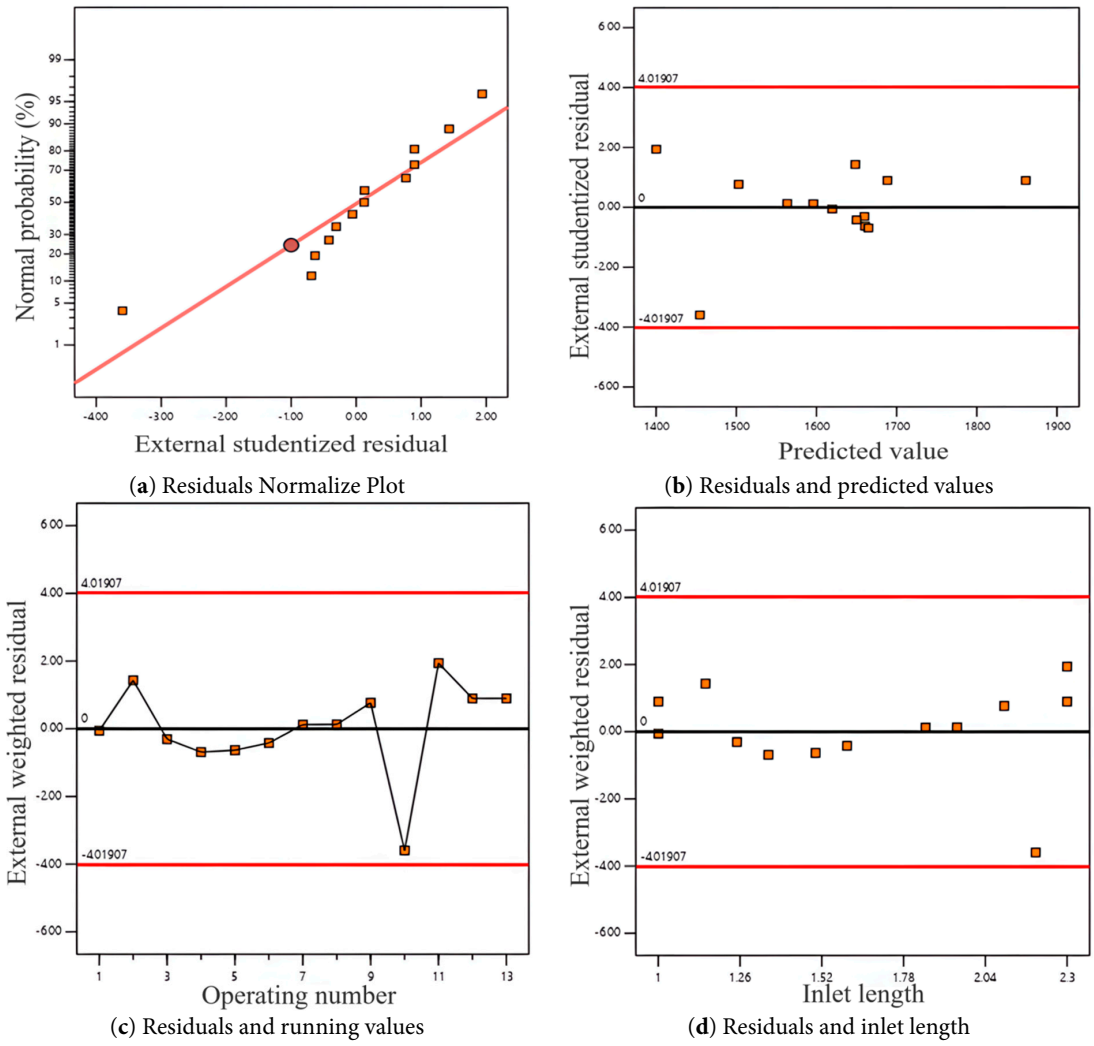

(**a**) Residuals Normalize Plot

(**b**) Residuals and predicted values

(**c**) Residuals and running values

(**d**) Residuals and inlet length

Figure 25: Residuals normalized heat transfer coefficient plot with predicted values.

3.4 Coupling Effect of Inlet Angle and Geometry

While the present study investigated inlet angle and geometry parameters independently, it is important to acknowledge that these parameters interact in practice. The optimal inlet angle may vary with different inlet aspect ratios (L_2/L_1). For instance, a larger inlet width (L_2) may accommodate a wider range of effective inlet angles by reducing flow resistance and stabilizing the jet attachment. Conversely, for narrow inlets, excessive inclination may exacerbate flow separation.

Preliminary analysis suggests that the interaction effect between θ and L_2 is more significant than that between θ and L_1. When $L_2 > 15$ mm, the heat transfer coefficient remains relatively insensitive to θ in the range of 5°–15°, indicating that a wide inlet provides geometric tolerance for angle optimization. However, for $L_2 < 12$ mm, the heat transfer coefficient drops sharply when $\theta > 10°$, suggesting a strong coupling effect under constrained inlet conditions.

Future work will systematically investigate these interactions using full factorial design or central composite design covering combined variations of θ, L_1, and L_2. The response surface model established in Section 3.3 can be extended to include the angle parameter as an additional factor, enabling multi-parameter optimization.

3.5 Influence of Engine Speed and Applicable Range

The present study was conducted at a fixed engine speed of 300 rpm, corresponding to a mean piston speed of approximately 3.5 m/s. This condition represents a low-to-medium speed operating point typical of urban driving cycles. It is important to acknowledge that engine speed significantly influences the oscillating flow characteristics within the cooling gallery.

At higher speeds (>1000 rpm), the increased inertial effects of reciprocating motion enhance oil splashing and turbulence, potentially altering the optimal inlet angle. Preliminary analysis suggests that the 10° optimal angle may decrease to 5°–8° at higher speeds because the stronger inertial forces reduce the need for inlet-directed momentum. Conversely, at lower speeds (<200 rpm), gravitational effects become more pronounced, and a larger inlet angle (12°–15°) may be required to ensure adequate oil penetration.

The optimized inlet geometry (L_1 = 2.3 mm, L_2 = 14.0 mm) is expected to maintain its superiority across a moderate speed range (200–800 rpm) because the short-and-wide design principle remains valid under varying oscillation intensities. However, extrapolation beyond this range requires caution, and dedicated studies at 600 rpm, 1000 rpm, and 1500 rpm are recommended for full-speed optimization.

The current optimization is therefore specifically applicable to medium-speed diesel engines and gasoline engines at partial load conditions. For high-performance engines operating at >5000 rpm, additional validation is necessary.

4 Conclusion

This paper conducts an in-depth investigation into the inlet structure of piston cooling oil passages, examining the inclination angle of the oil chamber inlet. Using the average heat transfer coefficient and instantaneous heat transfer coefficient across each wall surface area as evaluation criteria, the thermal characteristics of the oil passage walls under different structural parameters were studied. The principal conclusions are as follows:

(1) The inclined inlet modifies the oil flow direction, enhancing turbulence and improving heat transfer efficiency. An inlet angle of 10° achieves the best cooling performance, reducing the maximum piston temperature by 1.69°C and lowering the minimum temperature region by 28.34°C. However, excessive

angles induce over-turbulence and flow instability, leading to low-velocity or stagnation zones that diminish local heat transfer.

(2) Increasing the inlet width enhances oil flow and coverage, thereby improving heat transfer along the gallery wall. With L_1 = 1.15 mm and L_2 = 16.3 mm, the area-averaged heat transfer coefficients at all crank angles exceed those of other configurations, reaching a maximum of 1755.13 W/(m^2·K) at 270°CA.

(3) Using goal programming with the time-averaged heat transfer coefficient as the optimization objective, the optimal structural parameters were determined as L_1 = 2.3 mm and L_2 = 14.0 mm, yielding a coefficient of 1928.513 W/(m^2·K). The deviation from simulation results was 6.6%, within the acceptable range.

(4) The coupling effect between inlet angle and geometry warrants further investigation. Preliminary analysis indicates that wide inlets (L_2 > 15 mm) provide geometric tolerance for angle variation, while narrow inlets require stricter angle control.

(5) The optimized inlet structure is applicable for engine speeds in the range of 200–800 rpm. The influence of higher engine speeds on the optimal inlet angle and geometry warrants further investigation.

Acknowledgement: This work was supported by the Jiangsu Provincial Higher Education Basic Science (Natural Science) Research Project (22KJA470003).

Funding Statement: This work was supported by the Jiangsu Provincial Higher Education Basic Science (Natural Science) Research Project (22KJA470003).

Author Contributions: Fei Dong: Funding acquisition, Methodology, Project administration, Supervision, Writing—review & editing; Weichao Zhang: Data curation, Formal analysis, Investigation, Software, Validation, Writing—original draft, Writing—review & editing; Jiurui Zhao: Validation, Visualization; Tongwei Zhang: Methodology, Supervision, Validation, Visualization. All authors reviewed and approved the final version of the manuscript.

Availability of Data and Materials: The data that support the findings of this study are available within the paper.

Ethics Approval: Not applicable. This study involves computational fluid dynamics simulations only and does not include human or animal subjects.

Conflicts of Interest: The authors declare no conflicts of interest.

References

1. Xiong P, Mu Z, Li M, Deng L, Chen Y, Qiao X, et al. New method for evaluating the influence of the cooling gallery shape on the heat load of piston. Int Commun Heat Mass Transf. 2025;164:108887. [CrossRef].
2. Wang J, Deng X, Xie G, Lei J, Jia D. A transient numerical study for heat transfer and flow characteristics of dimpled piston cooling gallery of a diesel engine. Case Stud Therm Eng. 2023;45:102930. [CrossRef].
3. Liu Y, Lei J, Wang D, Deng X, Wen J, Jiang X. Research on the optimization design method of ribbed cooling galleries in lightweight steel pistons based on heat transfer performance. Appl Therm Eng. 2025;269:126098. [CrossRef].
4. Liu Y, Lei J, Wang B, Deng X, Sun D, Wang H. Experimental and simulation study on oscillating flow and heat transfer characteristics of the cooling gallery in steel pistons. Case Stud Therm Eng. 2024;58:104436. [CrossRef].
5. Yang H, Lei J, Wang C, Sun F, Deng X, Wen J, et al. Research on the oscillating flow and heat transfer of the cooling gallery inside a multi-material composite piston. Case Stud Therm Eng. 2025;68:105879. [CrossRef].
6. Du Y, Fei C, Qian Z, Zhu S, Shu Z, Zhou K. Simulation analysis of thermal insulation performance of diesel engine piston based on PEO and $La_2Zr_2O_7$ thermal barrier coating. Case Stud Therm Eng. 2024;59:104460. [CrossRef].

7. Sun YQ, Zhu YS, Luo XT, Yang GJ, Li CJ. Plasma sprayed $K_2Ti_6O_{13}$ as thermal barrier coatings with high thermal swing for diesel piston enabled by inter-splat bonding and porosity tailoring. Surf Coat Technol. 2024;483:130726. [CrossRef].
8. Muthusamy J, Panithasan MS, Venkadesan G, Mariappan M. Computational and experimental analysis of yttria stabilized zirconia thermal barrier coated pistons: impact on temperature distribution, microstructure, CRDI engine performance, emissions, and energy balance. Appl Therm Eng. 2025;267:125731. [CrossRef].
9. Gainey B, Lawler B. Thermal barrier coatings in compression ignition engines: analysis of combustion strategies and insights into convection vive. Therm Sci Eng Prog. 2025;59:103320. [CrossRef].
10. Qin S, Xu L, Jia B, Ren P, Zhang Z, Liu C, et al. Conjugate heat transfer simulation of the linear range extender: thermal design considerations for cooling strategy. Energy. 2025;318:134928. [CrossRef].
11. Malathi M, Herbert Mabel J, Easwaramoorthy D, Rajendran R. Ni-P SiC composite coatings on piston rings by plate and bumper technique and its tribological properties. Surf Eng. 2024;40(11–12):1063–78. [CrossRef].
12. Ge C, Zhang B, Xu X, Lyu X, Ma X, Li T, et al. Tribofilm distribution and tribological analysis of piston ring-cylinder liner interfaces under realistic engine conditions. Tribol Int. 2025;201:110250. [CrossRef].
13. Dhairiyasamy R, Gabiriel D. Performance and emission characteristics of Mahua oil biodiesel in low heat rejection diesel engines with retarded injection timing. Chem Thermodyn Therm Anal. 2025;17:100158. [CrossRef].
14. Mehtab R, Binti Mohd Zulkifli NW, Bin Mohd Sabri MF, Morina A, Bin Abdollah MF, Bin Amiruddin H, et al. Tribological properties of oil palm fiber-derived graphene coatings on piston ring; influence of hydrogen flow rate during CVD process. Wear. 2025;572:206054. [CrossRef].
15. Dizisaz M, Parast MSA, Azadi M. The method for impact analyzing of duplex plasma nitriding and DLC coatings on the cyclic performance of $16MnCr_5$ piston pin steel under plain and fretting fatigue testing. MethodsX. 2025;14:103164. [CrossRef].
16. Wang Y, Zhang K, Mu H, Zhao X, Zhang X, Hao S, et al. Theoretical investigation of the effect of thermal barrier coating on ammonia combustion of marine medium speed engine. Energy. 2025;322:135667. [CrossRef].
17. Yoshikawa T, Reitz RD. Development of an oil gallery cooling model for internal combustion engines considering the cocktail shaker effect. Numer Heat Transf Part A Appl. 2009;56(7):563–78. [CrossRef].
18. Torregrosa AJ, Broatch A, Olmeda P, Martín J. A contribution to film coefficient estimation in piston cooling galleries. Exp Therm Fluid Sci. 2010;34(2):142–51. [CrossRef].
19. Najafabadi MI, Mirsalim M, Hosseini V, Alaviyoun S. Experimental and numerical study of piston thermal management using piston cooling jet. J Mech Sci Technol. 2014;28(3):1079–87. [CrossRef].
20. Yu X, Yi D, Huang Y, Lu Y, Paul Roskilly A. Experimental investigation of two-phase flow and heat transfer performance in a cooling gallery under forced oscillation. Int J Heat Mass Transf. 2019;132:1306–18. [CrossRef].
21. Hamza M, Mei BA, Zuo Z. Effect of surface roughness on the oil distribution and the heat transfer coefficient for piston cooling gallery. Case Stud Therm Eng. 2022;33:101960. [CrossRef].
22. Kumar P, Kumar A, Chamoli S, Kumar M. Experimental investigation of heat transfer enhancement and fluid flow characteristics in a protruded surface heat exchanger tube. Exp Therm Fluid Sci. 2016;71:42–51. [CrossRef].
23. Narato P, Wae-hayee M, Kaewchoothong N, Nuntadusit C. Heat transfer enhancement and flow characteristics in a rectangular channel having inclined pin arrays mounted on the endwall surface. Int Commun Heat Mass Transf. 2021;122:105162. [CrossRef].
24. Leontiev AI, Kiselev NA, Vinogradov YA, Strongin MM, Zditovets AG, Burtsev SA. Experimental investigation of heat transfer and drag on surfaces coated with dimples of different shape. Int J Therm Sci. 2017;118:152–67. [CrossRef].
25. Liu Y, Li C, Jiang W, Yuan Y, Guo Z, Shi J. Optimization of thermal stress on the top surface of a particle-reinforced composite coated piston based on Kriging model. Case Stud Therm Eng. 2025;69:106061. [CrossRef].
26. Rengarajan S, Muhammed R, Rao VS, Kota M. Impact of zirconium oxide and tantalum carbide powder coatings by plasma spraying techniques on engine performance. Prot Met Phys Chem Surf. 2024;60(5):959–69. [CrossRef].
27. Zhang F, Wang Q, Shen H, Bai C, Li C, Tian D, et al. Effect of SiC concentration on the microstructure and anti-wear performance of electrodeposited Ni-SiC composite coatings constructed for piston ring application. Materials. 2025;18(5):1117. [CrossRef].

28. He W, Zhang J, Guo R, Pei C, Li H, Liu S, et al. Performance analysis and structural optimization of a finned liquid-cooling radiator for chip heat dissipation. Appl Energy. 2022;327:120048. [CrossRef].
29. Dong F, Zhao JR, Zhang WY. Numerical study of the influence of wetting properties on flow characteristics and heat transfer in piston cooling gallery. Proc Inst Mech Eng Part D J Automob Eng. 2025;239(9):4062–77. [CrossRef].